



# Protoplanetary Disk Polarization at Multiple Wavelengths: Are Dust Populations Diverse?

Rachel E. Harrison<sup>1,2</sup>, Zhe-Yu Daniel Lin<sup>3</sup>, Leslie W. Looney<sup>1</sup>, Zhi-Yun Li<sup>3</sup>, Haifeng Yang<sup>4</sup>, Ian W. Stephens<sup>5</sup>, and Manuel Fernández-López<sup>6</sup>

<sup>1</sup> Department of Astronomy, University of Illinois, Urbana, IL 61801, USA; [reh3@illinois.edu](mailto:reh3@illinois.edu)

<sup>2</sup> School of Physics and Astronomy, Monash University, Vic 3800, Australia

<sup>3</sup> Department of Astronomy, University of Virginia, Charlottesville, VA 22904, USA

<sup>4</sup> Kavli Institute for Astronomy and Astrophysics, Peking University, Yi He Yuan Lu 5, Haidian Qu, Beijing 100871, People's Republic of China

<sup>5</sup> Department of Earth, Environment and Physics, Worcester State University, Worcester, MA 01602, USA

<sup>6</sup> Instituto Argentino de Radioastronomía (CCT-La Plata, CONICET; UNLP; CICPBA), C.C. No. 5, 1894, Villa Elisa, Buenos Aires, Argentina

Received 2023 March 2; revised 2024 March 17; accepted 2024 April 1; published 2024 May 16

## Abstract

Millimeter and submillimeter observations of continuum linear dust polarization provide insight into dust grain growth in protoplanetary disks, which are the progenitors of planetary systems. We present the results of the first survey of dust polarization in protoplanetary disks at 870  $\mu\text{m}$  and 3 mm. We find that protoplanetary disks in the same molecular cloud at similar evolutionary stages can exhibit different correlations between observing wavelength and polarization morphology and fraction. We explore possible origins for these differences in polarization, including differences in dust populations and protostar properties. For RY Tau and MWC 480, which are consistent with scattering at both wavelengths, we present models of the scattering polarization from several dust grain size distributions. These models aim to reproduce two features of the observational results for these disks: (1) both disks have an observable degree of polarization at both wavelengths; and (2) the polarization fraction is higher at 3 mm than at 870  $\mu\text{m}$  in the centers of the disks. For both disks, these features can be reproduced by a power-law distribution of spherical dust grains with a maximum radius of 200  $\mu\text{m}$  and high optical depth. In MWC 480, we can also reproduce features (1) and (2) with a model containing large grains ( $a_{\text{max}} = 490 \mu\text{m}$ ) near the disk midplane and small grains ( $a_{\text{max}} = 140 \mu\text{m}$ ) above and below the midplane.

*Unified Astronomy Thesaurus concepts:* [Protoplanetary disks \(1300\)](#); [Polarimetry \(1278\)](#)

## 1. Introduction

Polarized emission from dust on protoplanetary disks has been observed at millimeter and submillimeter wavelengths in an increasing number of sources. Multiple mechanisms could theoretically produce this polarized emission, including the alignment of nonspherical dust grains to the magnetic field (e.g., Lazarian 2007) or radiation anisotropy (Tazaki et al. 2017), aerodynamic alignment due to gas–dust interactions (Gold 1952; Yang et al. 2019), or self-scattering of thermal dust emission (e.g., Kataoka et al. 2015; Yang et al. 2016, 2017). Multiwavelength polarization observations are necessary to distinguish between these mechanisms and to extract information about dust properties from the polarized emission.

Because magnetic fields are thought to be critical to the accretion process, one of the initial goals of polarization studies of protoplanetary disks was to use polarized emission from grains aligned to the magnetic field to trace the field's morphology (e.g., Rao et al. 2014; Stephens et al. 2014; Segura-Cox et al. 2015). However, with a small number of possible exceptions (e.g., Alves et al. 2018; Ohashi et al. 2018; Sadavoy et al. 2018), the polarized emission seen in most disks does not match the pattern that would be produced by dust grains aligning to magnetic field morphologies predicted by

theory. Instead, the polarization seen in many disks is better explained by other mechanisms.

In an inclined axisymmetric disk, the collective scattering of thermal photons from dust grains by other dust grains produces polarization that is parallel to the disk minor axis (Kataoka et al. 2015; Yang et al. 2016). This pattern, indicative of scattering, has been observed in several sources (e.g., Stephens et al. 2017; Bacciotti et al. 2018; Dent et al. 2019). Scattering polarization fractions can be up to a few percent if most of the grains are in the Rayleigh scattering regime (i.e., much smaller than the observing wavelength). For a given observing wavelength, the polarization fraction from scattering is highly dependent on the maximum dust grain size. The polarization fraction peaks when the maximum grain size is of order  $\lambda/2\pi$ , where  $\lambda$  is the observing wavelength (Kataoka et al. 2015). Therefore, observing the scattering polarization spectrum of a source can constrain the maximum grain size. In addition to the dust grain size, the disk inclination, optical depth, and dust scale height can all affect the level of polarization from scattering (e.g., Yang et al. 2017; Ohashi & Kataoka 2019; Brunngräber & Wolf 2020).

Polarization patterns not consistent with pure scattering have also been observed in some protoplanetary disks at millimeter wavelengths. At 3 mm, HL Tau, DG Tau, and Haro 6-13 all exhibit an azimuthal polarization pattern that likely arises from primarily thermal emission by aligned, elongated dust grains (Stephens et al. 2017; Harrison et al. 2019). Several mechanisms have been proposed for grain alignment, including alignment to the magnetic field or radiation anisotropy through radiative alignment torques (RATs; Tazaki et al. 2017) and

**Table 1**  
Disk Parameters

Source	$M_*$ ( $M_\odot$ )	$L_*$ ( $L_\odot$ )	Age (Myr)	Inc. (deg)	Dist. (pc)	References
Haro 6-13	$1.00 \pm 0.15$	0.79	2.60	38	130.4	(1, 2, 3)
MWC 480	1.91	17.38	6.90	36.5	161	(4)
RY Tau	2.04	12.30	5.00	65.0	128	(4)
V892 Tau	$6.0 \pm 0.2^a$	128.82	0.79	54.5	134.5	(5, 6)
DL Tau	0.98	0.65	3.50	45.0	159	(4)

**Notes.** Masses, inclinations, and distances for the sources in this survey. A disk inclination of  $0^\circ$  is defined as face-on, and an inclination of  $90^\circ$  is defined as edge-on. Distances are from Gaia parallax measurements (Gaia Collaboration et al. 2016, 2018).

<sup>a</sup> Combined mass of binary.

**References.** (1) Schaefer et al. (2009); (2) Garufi et al. (2021); (3) Long et al. (2019); (4) Long et al. (2018); (5) Long et al. (2021); and (6) Herczeg & Hillenbrand (2014).

**Table 2**  
Ring and Gap Radii, in Astronomical Units

Source	Ring 1	Ring 2	Ring 3	Gap 1	Gap 2	Gap 3
MWC 480	$97.58 \pm 0.08$	...	...	$73.43 \pm 0.16$	...	...
RY Tau	$18.19 \pm 0.00$	$49.04 \pm 0.14$	...	$43.41 \pm 0.13$	...	...
V892 Tau	$26.90 \pm 0.14$	...	...	...	...	...
DL Tau	$46.44 \pm 0.48$	$78.08 \pm 0.24$	$112.27 \pm 0.32$	$39.29 \pm 0.32$	$66.95 \pm 0.87$	$88.90 \pm 0.11$

**Note.** Radii of known rings and gaps, assuming the distances in Table 1. The data for MWC 480, RY Tau, and DL Tau are from Long et al. (2018). The data for V892 Tau are from Long et al. (2021).

mechanical alignment (Gold 1952; Kataoka et al. 2019; Yang et al. 2019). HL Tau’s polarization spectrum is particularly interesting: the disk’s polarization morphology transitions from a pattern consistent with scattering at  $\sim 870 \mu\text{m}$  to an elliptical pattern at  $\sim 3 \text{ mm}$ , with an intermediate pattern at  $\sim 1.3 \text{ mm}$  (Stephens et al. 2017). Recently, Lin et al. (2022) and Lin et al. (2024) have demonstrated that HL Tau’s polarization spectrum could be explained by polarization from thermal emission and the scattering of aligned grains, also demonstrating that the polarization seen at high resolution in HL Tau at  $870 \mu\text{m}$  could be explained by the same mechanisms. At longer wavelengths, thermal polarization dominates because the low optical depth makes scattering inefficient. At shorter wavelengths, scattering polarization dominates because the high optical depth makes scattering events frequent and dichroic extinction decreases the contribution from thermal polarization (Lin et al. 2022).

The changes in polarization with wavelength seen in HL Tau invite the question of whether other disks exhibit similar polarization patterns at these wavelengths. Harrison et al. (2019) have demonstrated that otherwise similar protoplanetary disks can exhibit different polarization morphologies at the same observing wavelength. The polarized emission in the Class II protoplanetary disks observed at  $3 \text{ mm}$  with the Atacama Large Millimeter/submillimeter Array (ALMA) in Harrison et al. (2019) can be qualitatively split into two categories: those with polarization consistent with scattering (RY Tau, MWC 480, and potentially DL Tau) and those with azimuthally oriented polarization vectors (DG Tau, Haro 6-13, and V892 Tau). Given how strongly scattering is affected by grain size with respect to the observing wavelength and how thermal polarization from aligned grains depends on the optical depth, differences in the polarization spectra could indicate differences in the grain sizes and conditions of grain alignment. These dust grains are the building blocks of potential planets in such systems. We present the results of total intensity and

continuum linear polarization observations of five Class II disks at  $870 \mu\text{m}$  and  $3 \text{ mm}$ : Haro 6-13, MWC 480, RY Tau, DL Tau, and V892 Tau. With these observations, we have significantly expanded the number of protoplanetary disks observed in polarization at multiple wavelengths.

## 2. Observations

We observed DL Tau, Haro 6-13, RY Tau, MWC 480, and V892 Tau at  $870 \mu\text{m}$  (ALMA Band 7). These sources are all Class II disks located in the Taurus Molecular Cloud. The disks surround low-mass protostars with a range of ages, luminosities, and masses. The disks of DL Tau, Haro 6-13, RY Tau, and MWC 480 all surround single stars, while V892 Tau is a circumbinary disk around a close binary with a third stellar object orbiting outside the disk (Long et al. 2021). Protostar masses, luminosities, ages, disk inclinations, and distances are listed in Table 1. Table 2 lists the radii of known rings and gaps in the disks.

The observations were taken with ALMA between 2018 September 18 and September 19 in configuration C43-4. The observations were at a frequency range of 337.48–349.51 GHz (ALMA Band 7). J0438+3004 was the phase calibrator, J0522–3627 was the polarization calibrator, and J0510+1800 was the bandpass and flux calibrator.

The data sets were calibrated by data analysts at the North American ALMA Science Center. After this initial calibration, we performed three rounds of phase-only self-calibration on all Stokes parameters ( $I$ ,  $Q$ ,  $U$ , and  $V$ ). The gain calibration solution interval was equal to the scan length for the first round of self-calibration, 30 s for the second round, and 15 s for the third round. We used the CASA task `telean` with `stokes = "IQUV,"` Briggs weighting, and a robust parameter of 0.5. Polarization angle and intensity maps were produced from the Stokes  $Q$  and  $U$  data. The polarized intensity maps were debiased using the average noise value determined from

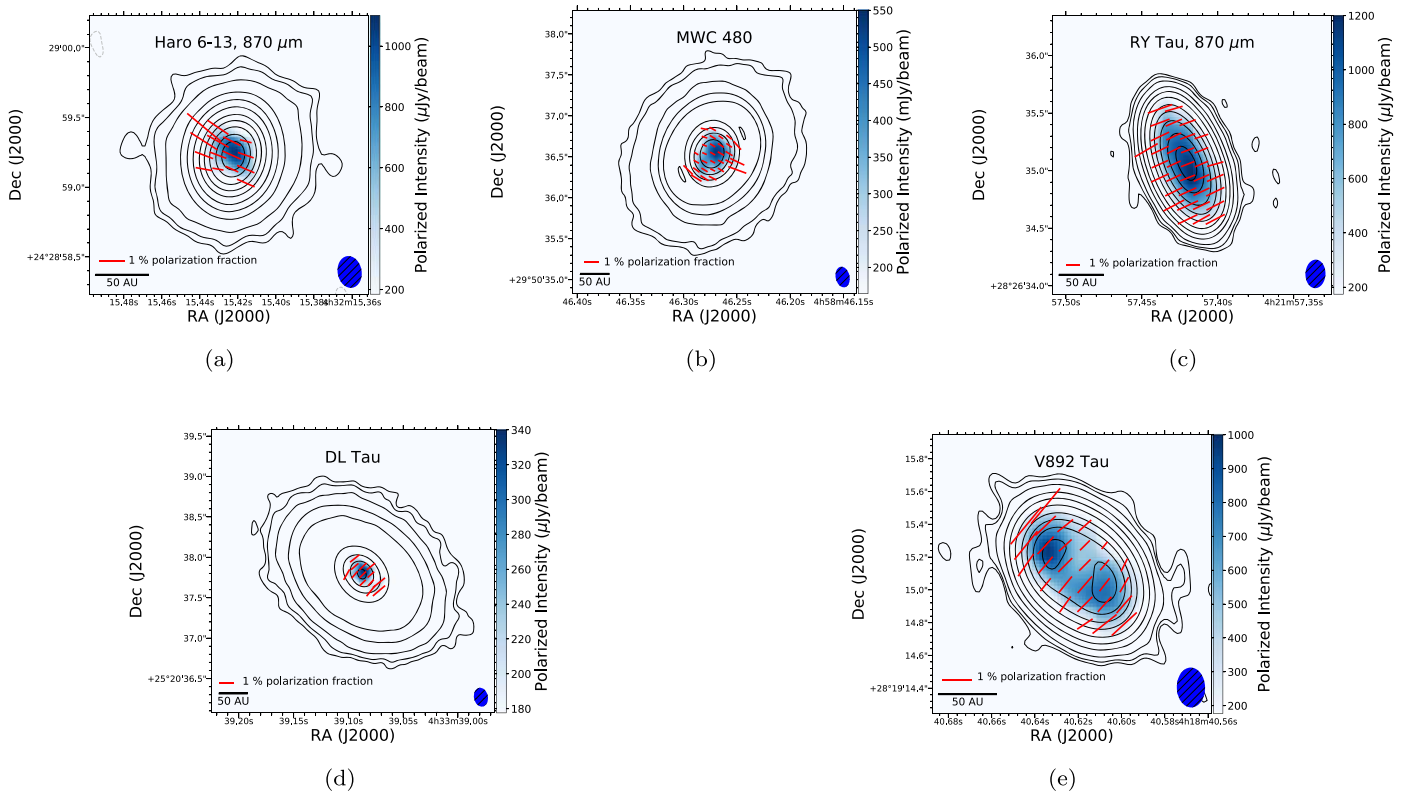


**Figure 1.** Images of Haro 6-13, MWC 480, RY Tau, DL Tau, and V892 Tau at  $870 \mu\text{m}$ . The contours represent the total intensity (Stokes  $I$ ) at  $-3\sigma$  (dashed),  $3\sigma$ ,  $10\sigma$ ,  $50\sigma$ ,  $100\sigma$ ,  $250\sigma$ ,  $325\sigma$ ,  $500\sigma$ ,  $750\sigma$ ,  $1000\sigma$ , and  $1500\sigma$  levels, where  $\sigma$  is listed in Table 3. The color map represents the polarized intensity with the scale on the right of each source and is shown where the polarized intensity is  $>3\sigma_p$ . The length of the polarization vectors corresponds to the polarization fraction. The vectors are plotted with  $\sim$ three segments per beam and are plotted in regions where  $P$  and  $I$  are both  $>3\sigma$ .

the  $Q$  and  $U$  maps, an estimator used by, e.g., Wardle & Kronberg (1974) and Vidal et al. (2016):

$$P = \begin{cases} \sqrt{Q^2 + U^2 - \sigma^2} & \text{if } \sqrt{Q^2 + U^2} \geq \sigma \\ 0 & \text{otherwise} \end{cases} \quad (1)$$

While V892 Tau and DL Tau were reported as unpolarized at 3 mm in Harrison et al. (2019), upon closer examination we found that small regions of these disks were polarized at the  $>3\sigma$  level. V892 Tau exhibits azimuthal polarization at 3 mm.

DL Tau has a polarized region near the center of the disk that is less than half the size of the beam, and the peak polarized intensity is  $3.5\sigma_p$ . This region's peak polarization fraction is 0.9%, and the direction of polarization is along the disk's minor axis. DL Tau also has several smaller polarized regions outside the disk center with polarization fractions up to 30%, whose direction of polarization angle is along the disk's minor axis. The polarized regions in DL Tau are so small that few independent measurements of the polarization angle can be made. Higher-sensitivity observations will be needed to determine whether this tentative polarization detection is real. We also note that while the majority of the polarized emission at Band 3 in MWC 480 is consistent with scattering, with the angle of polarization along the disk minor axis, there are two sub-beam-sized regions of polarized emission  $>3\sigma$  in the outer part of the disk whose polarization angles are not along the minor axis. It is possible that these nonscattering polarized regions arise from aligned grains; however, they do not form a complete ring, as the azimuthally oriented polarized emissions in DG Tau, Haro 6-13, and HL Tau do at 3 mm.

The images have angular resolutions between  $0''.2$  and  $0''.3$ . The uncertainty on absolute flux calibrations with ALMA is estimated at  $\sim 10\%$ . ALMA's instrumental limit for a  $3\sigma$  detection of polarized emission is 0.1% polarization for compact sources within one-third of the primary beam. The typical sensitivities of the Stokes  $Q$  and  $U$  images are about  $50\text{--}60 \mu\text{Jy beam}^{-1}$ . For the rest of this paper, only statistical uncertainties are considered.

### 3. Results

Here, we describe the results of the  $870 \mu\text{m}$  observations and compare them to the polarized emission observed in the same sources at 3 mm in Harrison et al. (2019). At  $870 \mu\text{m}$ , all five disks exhibit polarization morphologies consistent with scattering, regardless of the stellar mass, age, luminosity, multiplicity, or polarization at 3 mm. Figure 1 shows the total intensity, polarized intensity, polarization angle, and polarization fraction for the five disks at  $870 \mu\text{m}$ . Other observations of protoplanetary disks at  $870 \mu\text{m}$  (e.g., Stephens et al. 2017; Bacciotti et al. 2018; Dent et al. 2019) and 1.3 mm (Sadavoy et al. 2019) have found that scattering polarization is fairly common at these wavelengths. This indicates that the dust in these sources has grown large enough to produce scattering polarization at wavelengths of  $\sim 1 \text{ mm}$  (likely a few hundred microns, assuming the grains are compact and spherical). These disks must also be optically thick enough ( $\tau \gtrsim 1$ ) at the observed wavelengths to produce an observable polarization fraction.

Table 3 lists the measured values for total intensity (as determined from a Gaussian fit to the source) and peak polarized intensity, as well as the beam size. Figure 1 shows

**Table 3**  
Total and Polarized Intensities and rms Values, Peak Percent Polarization, and Beam Sizes

Source	$I$ Flux (mJy)	$I$ Peak (mJy $\text{bm}^{-1}$ )	$\sigma_I$ ( $\mu\text{Jy } \text{bm}^{-1}$ )	$P$ Peak ( $\mu\text{Jy } \text{bm}^{-1}$ )	$\sigma_P$ ( $\mu\text{Jy } \text{bm}^{-1}$ )	Peak % $P$	Beam FWHM
Haro 6-13	$339 \pm 1$	130.2	102	1074	61.6	1.9	$0''.230 \times 0''.172$
MWC 480	$598 \pm 16$	131.7	176	540	54.8	1.6	$0''.254 \times 0''.170$
RY Tau	$570 \pm 6$	111.9	98.4	1197	58.1	3.2	$0''.248 \times 0''.174$
V892 Tau	$745 \pm 44$	137.5	152	968	59.6	2.0	$0''.244 \times 0''.172$
DL Tau	$310 \pm 17$	53.9	98.9	340	59.2	1.3	$0''.235 \times 0''.173$

**Table 4**  
Angular Resolutions of Smoothed Data

Source	Beam (3 mm)
Haro 6-13	$0''.27 \times 0''.22$
MWC 480	$0''.33 \times 0''.26$
RY Tau	$0''.43 \times 0''.30$
V892 Tau	$0''.25 \times 0''.25$
DL Tau	$0''.31 \times 0''.28$

composite images of the Stokes  $I$  and polarized emission observed in Haro 6-13, MWC 480, RY Tau, DL Tau, and V892 Tau at  $870 \mu\text{m}$ . The contours indicate the total intensity of the dust emission in multiples of  $\sigma$ , and the blue shading indicates the polarized intensity. The red lines indicate the polarization angle and are scaled to correspond to the polarization fraction. We refer to these lines as “vectors,” though there is a  $180^\circ$  ambiguity in their direction.

Figure 2 shows the polarization fractions and angles for each disk detected in polarization at both 3 mm and  $870 \mu\text{m}$ . The vectors are superimposed on the Stokes  $I$  contours at  $870 \mu\text{m}$  from Figure 1. The data in Figure 2 have been smoothed to the same resolution. For Haro 6-13, MWC 480, and RY Tau, the  $870 \mu\text{m}$  data have been smoothed to the resolution of the 3 mm data. The negative bowl seen around MWC 480 is also present in the nonsmoothed data and may be due to large-scale structure being resolved out. The V892 Tau data from both bands have been smoothed to a resolution of  $0''.25$ ; this resolution is slightly larger than the major and minor axes of the beams at 3 mm and  $870 \mu\text{m}$ . The angular resolutions of the data in Figure 2 are listed in Table 4.

Polarized emission was not detected in the center of V892 Tau’s disk at 3 mm. We examined the possibility that nonthermal emission could affect the observed polarization fraction. Since only thermal emission contributes to polarized emission by scattering, contamination from nonthermal emission could reduce the observed polarization fraction. Long et al. (2021) observed a spectral index of  $\sim 0$  in V892 Tau between 8 and 9.8 mm near the center of the disk, which they report may be due to free-free emission from ionized gas. Hamidouche (2010) estimated the contamination from free-free emission in V892 Tau to be 10% at 2.7 mm. If the level of contamination is similar at 3 mm, then the free-free emission would only lower the observed polarization fraction by  $\sim 0.1\%$ , which is at the threshold of ALMA’s polarization detection limits. If the azimuthally oriented polarization pattern continues in the center of V892 Tau, beam-smearing effects are a more likely explanation for the lack of polarized emission in the disk’s center.

We calculated the average values of the spectral index ( $\alpha$ ) in a region at the centers of the disks with an area equivalent to the beam FWHM in Table 4. The average values of  $\alpha$  at the centers of the disks were 2.0 for Haro 6-13, 2.5 for MWC 480, 2.3 for

RY Tau, and 2.3 for V892 Tau. There was no obvious correlation between the spectral indices at the centers of the disks and their polarization spectra. These values of  $\alpha$  are consistent with the disk either being optically thick in the center or having small  $\beta$ . Figure 3 shows the radial profiles of the spectral index along the disks’ major and deprojected minor axes. Full optical depth modeling of these disks would require high-resolution observations that resolved disk substructure, namely rings and gaps, since disk substructure can significantly affect both the spectral index and polarization fraction and morphology.

Figures 4 and 5 show the polarization fractions of each disk versus distance from the Stokes  $I$  center along the disks’ major and deprojected minor axes, respectively. In Haro 6-13, MWC 480, RY Tau, and DL Tau, the Stokes  $I$  center is defined as the location of the Stokes  $I$  peak. In V892 Tau, the Stokes  $I$  center is defined as the midpoint between the two Stokes  $I$  peaks. Each point in the plots represents the average value of a line of pixels the length of one-half of the beamwidth projected along the major and minor axes. To determine the values of the points, we calculated the average values of  $I$ ,  $Q$ , and  $U$  in each half-beamwidth line of pixels along each axis, then calculated the percent polarization  $p$  as

$$p = \frac{100}{I} \sqrt{Q^2 + U^2}. \quad (2)$$

To determine the uncertainties on  $I$ ,  $Q$ , and  $U$ , we calculated the average value of 16 rectangular regions half the size of the beam in regions of the image outside of any emission. We take the variance of those means as the uncertainty on the average values of  $I$ ,  $Q$ , and  $U$ . We calculate the uncertainty on the percent polarization,  $\sigma_p$ , as

$$\sigma_p = \frac{100}{I} \left( \frac{1}{(Q^2 + U^2)} [(Q\sigma_Q)^2 + (U\sigma_U)^2] + \left[ \left( \frac{Q}{I} \right)^2 + \left( \frac{U}{I} \right)^2 \right] \sigma_I^2 \right)^{1/2}.$$

The debiased percent polarization,  $p'$ , which is plotted in Figures 4 and 5, is calculated as

$$p' = \sqrt{p^2 - \sigma_p^2}. \quad (3)$$

In disks known to have rings and gaps, ring locations are indicated by the solid vertical lines and gap locations are indicated by the dashed vertical lines. The black scale bar indicates the beam size in the smoothed images.

It is immediately clear from Figure 2 that the disks in this survey exhibit two different morphological groups across two wavelengths. Of the four disks in which we have observed polarized emission at the  $3\sigma$  level at 3 mm and  $870 \mu\text{m}$ , Haro 6-13 and V892 Tau show a transition of polarization patterns similar to HL Tau at the same wavelengths, while MWC 480

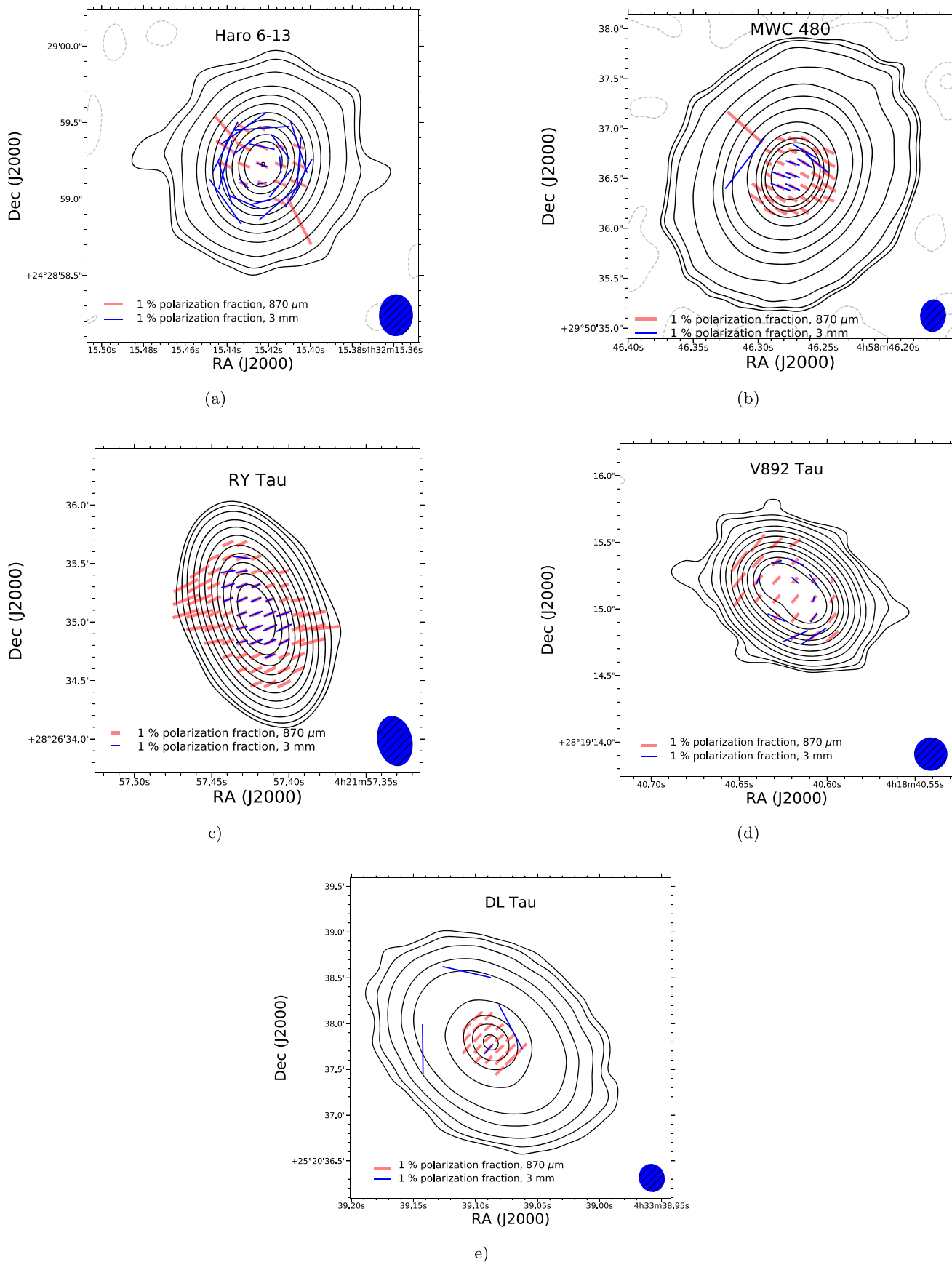


**Figure 2.** Images of Haro 6-13, MWC 480, RY Tau, V892 Tau, and DL Tau showing the polarization angles at 870  $\mu\text{m}$  (red lines) and 3 mm (blue lines). The black contours represent Stokes  $I$  at levels of  $-3\sigma$  (dashed),  $3\sigma$ ,  $10\sigma$ ,  $50\sigma$ ,  $100\sigma$ ,  $250\sigma$ ,  $325\sigma$ ,  $500\sigma$ ,  $750\sigma$ ,  $1000\sigma$ , and  $1500\sigma$ , where  $\sigma$  is the rms of the smoothed 870  $\mu\text{m}$  images. Vectors are plotted in regions where the total intensity and polarized intensity are both  $>3\sigma$ . The length of the vectors is scaled with percent polarization up to a threshold of 3% to better show the variation at low polarization fraction. The blue ellipse represents the beam size.

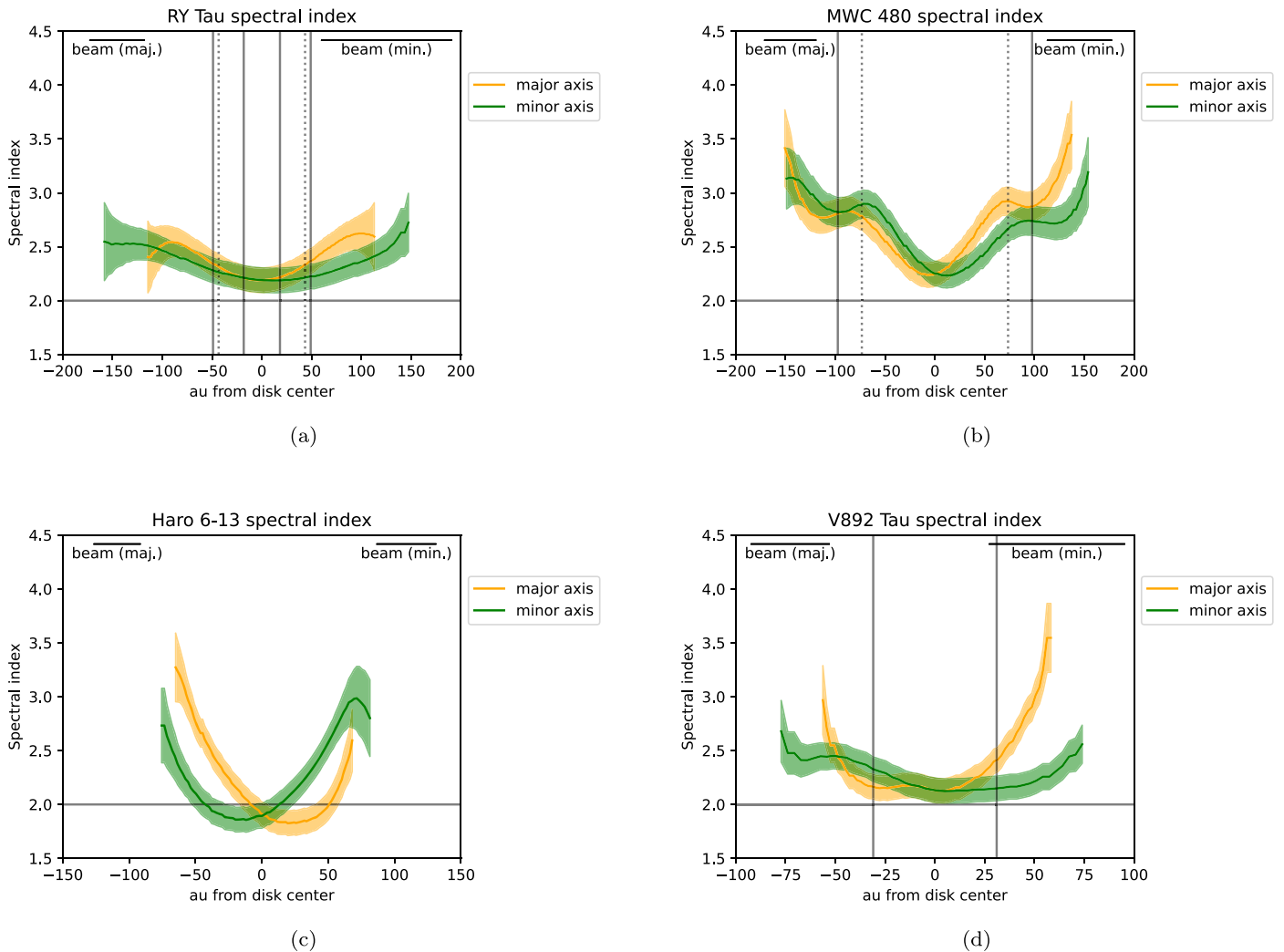


**Figure 3.** Spectral indices along the disks’ major and minor axes. The shaded regions represent  $1\sigma$  error bars, including the 10% uncertainty on the absolute flux value. The gray horizontal line represents  $\alpha = 2$ .

and RY Tau show polarization patterns indicative of scattering at both wavelengths (i.e., polarization vectors well aligned to the disk minor axis, as described in Yang et al. 2016). Additionally, we observed polarization consistent with scattering at  $870\ \mu\text{m}$  in DL Tau.

One notable feature of the polarization spectra of RY Tau and MWC 480 is the relative polarization fractions at the two wavelengths. Both wavelengths have polarization fractions  $>0.4\%$ , with a higher polarization fraction at 3 mm in the center of the disk. This is in contrast to previous scattering models, such as those presented in Kataoka et al. (2017), which predict a steep correlation between polarization fraction and observing wavelength. In the scattering polarization models for RY Tau and MWC 480 discussed in Section 4, we have aimed to reproduce an observable degree of scattering polarization at both observing wavelengths and a higher polarization fraction at 3 mm in the center of the disk.

#### 4. Discussion

The morphological differences in the polarization spectra of our sources are of interest because they may point toward differences in the disks’ dust environments and/or correlations between polarization and protostar properties. Dust grain

sizes and optical depths affect the degree of scattering polarization observed, as well as whether polarization from scattering or from aligned grains dominates. In Section 4.1, we compare the data from RY Tau and MWC 480 to models of the scattering polarization for various dust grain populations. In Section 4.2, we explore possible causes of the differences in polarization morphology transitions between the two wavelengths.

Because the scattering efficiency at a given wavelength is heavily dependent on dust grain size (Kataoka et al. 2015), the polarization fraction from scattering is expected to vary significantly with observing wavelength for a disk whose dust grain sizes are defined by a simple power-law distribution (Kataoka et al. 2017). However, MWC 480 and RY Tau show a fairly similar degree of scattering polarization at two widely separated observing wavelengths. There are several scenarios that could give rise to the significant degree of polarization in these sources at  $870\ \mu\text{m}$  and 3 mm, including:

1. *Optical depth effects.* The dust is well described by a single population with a defined maximum grain size. The polarization fraction depends on the optical depth, which differs at different wavelengths. In the optically thin limit, the polarization fraction increases with

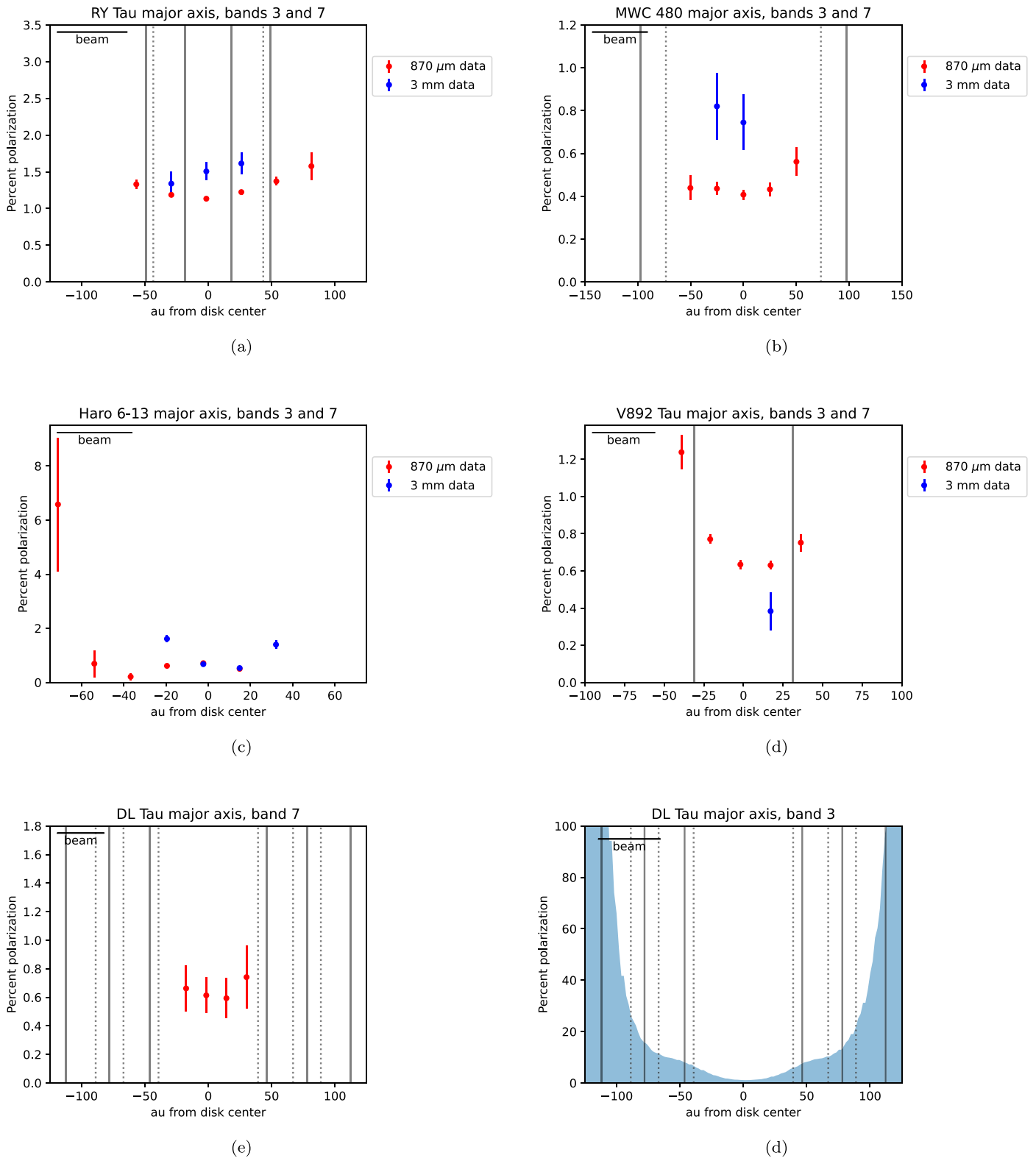


**Figure 4.** Percent polarization vs. distance from disk center along the disk major axis at 3 mm and 870  $\mu\text{m}$  for RY Tau, MWC 480, Haro 6-13, and V892 Tau, and at 870  $\mu\text{m}$  for DL Tau. For RY Tau, MWC 480, Haro 6-13, and V892 Tau, the two bands have been smoothed to the same resolution; the scale bar indicates the beam size. The smoothed resolutions are listed in Table 4. For DL Tau, we show the 870  $\mu\text{m}$  data at the resolution listed in Table 3. Since the polarized region in DL Tau at 3 mm was less than half of the beam FWHM across, we have plotted the  $3\sigma$  upper limit on the percent polarization in DL Tau at 3 mm. The resolution at 3 mm is listed in Table 4. The data are only plotted in regions where the polarized intensity is at least  $3\sigma_p$ . The solid vertical lines indicate the locations of known rings, and the dotted vertical lines indicate the locations of known gaps.

increasing optical depth. The polarization peaks when the optical depth is of order unity, after which it decreases to a constant value in the optically thick limit (Yang

et al. 2017). If the disk is optically thick at 870  $\mu\text{m}$ , optical depth effects would attenuate the scattering polarization at that wavelength.

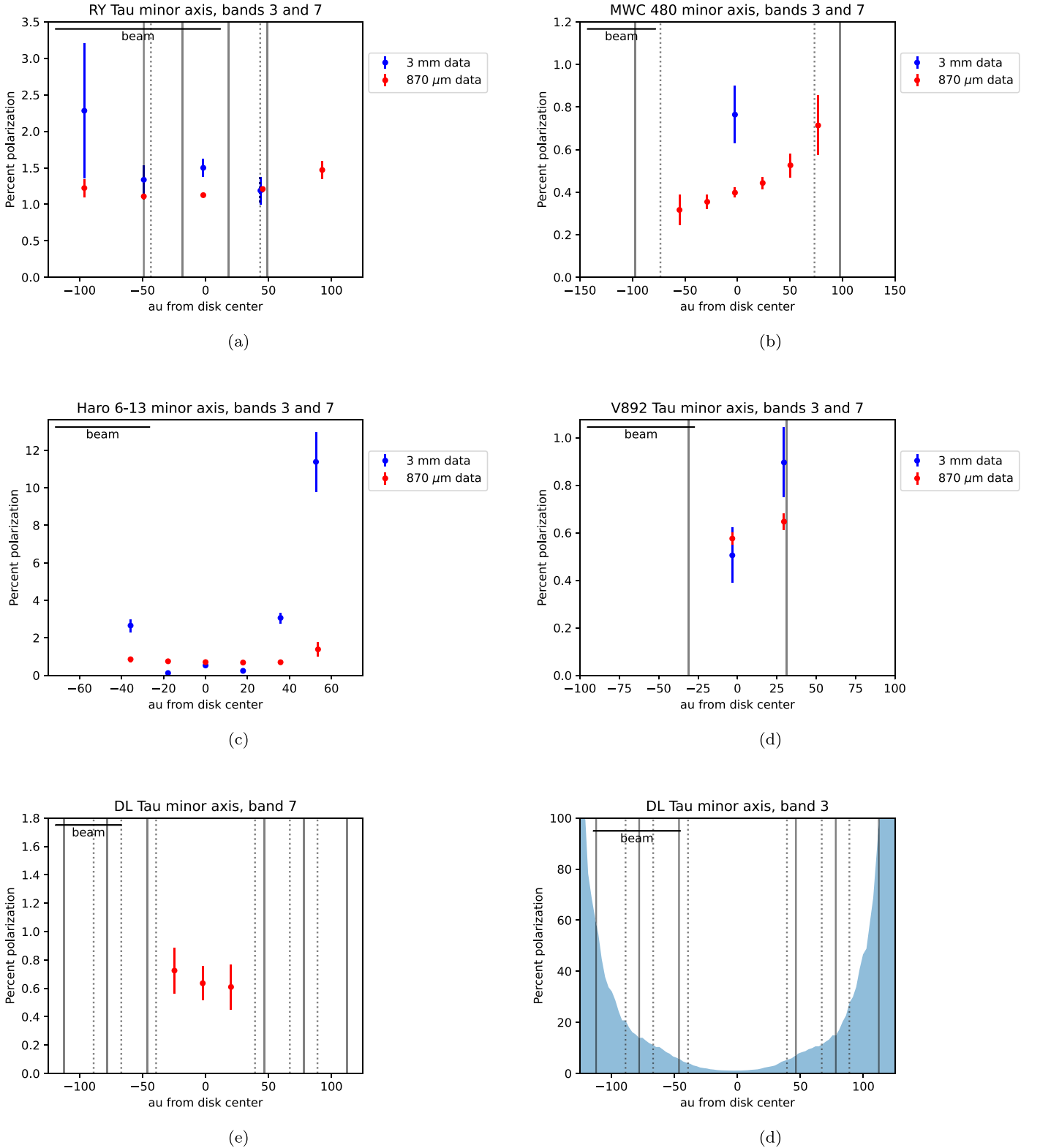


**Figure 5.** Percent polarization vs. distance from disk center along the disk deprojected minor axis at 3 mm and 870  $\mu\text{m}$  for RY Tau, MWC 480, Haro 6-13, and V892 Tau, and at 870  $\mu\text{m}$  for DL Tau. For RY Tau, MWC 480, Haro 6-13, and V892 Tau, the two bands have been smoothed to the same resolution; the scale bar indicates the beam size. The smoothed resolutions are listed in Table 4. For DL Tau, we show the 870  $\mu\text{m}$  data at the resolution listed in Table 3. Since the polarized region in DL Tau at 3 mm was less than half of the beam FWHM across, we have plotted the  $3\sigma$  upper limit on the percent polarization in DL Tau at 3 mm. The resolution at 3 mm is listed in Table 4. The data are only plotted in regions where the polarized intensity is at least  $3\sigma_p$ . The solid vertical lines indicate the locations of known rings, and the dotted vertical lines indicate the locations of known gaps.

2. *Multiple dust grain populations.* The disks contain multiple dust grain populations with different maximum sizes. The vertical component of the stellar gravity pulls

the grains toward the disk midplane, causing them to settle, and this effect is stronger for larger grains (Barrière-Fouchet et al. 2005). The larger grains dominate



the optical depth at longer wavelengths, whereas the smaller grains are effectively invisible and do not contribute to polarization. At shorter wavelengths, an increase in the optical depth of the smaller grains that are elevated can screen out emission of the large grains near the midplane (Ueda et al. 2021), meaning that the scattering polarization from smaller grains above the midplane would dominate.

3. *Dust grain porosity.* The dust grains in the disk are highly porous. Scattering from porous dust grains leads to a flatter polarization spectrum than scattering from nonporous grains (see, e.g., Figure 10 of Tazaki et al. 2019).
4. *Disk substructure.* Ring/gap structures in the disk create radial variations in optical depth. These variations in optical depth then affect the observed polarization fraction from scattering, as described in Lin et al. (2020).

Investigating the effects of disk substructure on these sources' polarization spectra will require higher-resolution observations. At the native resolution of the 870  $\mu\text{m}$  images, only the ring and gap in MWC 480 are resolved. Higher-sensitivity observations will also be necessary to explore the effects of disk substructure; the polarized region of MWC 480 only extends to the disk's gap, and higher-sensitivity observations would reveal fainter polarized emission at larger radii. Since dust porosity is poorly constrained and disk substructure is not well resolved in our sources, we will explore only scenarios 1 and 2 further, in Section 4.1, by comparing the 3 mm and 870  $\mu\text{m}$  data to models of the polarized emission produced by scattering for several different dust grain populations.

#### 4.1. Scattering Models

Since MWC 480 and RY Tau show evidence of pure scattering at both wavelengths, we explore models of these two sources' polarization in this section. While determining the precise dust grain distribution that best fits the data is beyond the scope of this paper, we aim to show that dust settling and optical depth effects should be taken into account when using scattering polarization observations to constrain a disk's dust properties. The key features we aim to reproduce in the models are: (1) a significant degree ( $\sim 0.5\%$ – $2\%$ ) of polarization at observing wavelengths of both 3 mm and 870  $\mu\text{m}$ ; and (2) a higher polarization fraction for 3 mm than 870  $\mu\text{m}$  in the center of the disk. These features are of particular interest because they differ from the predictions of simple scattering models, such as those in Kataoka et al. (2017). Given that polarization due to scattering depends on inclination (Yang et al. 2016), we use the two inclination angles for the two sources.

Modeling the scattering polarization for a range of dust populations will help to determine promising avenues for future modeling to further constrain the dust grain sizes in RY Tau and MWC 480. Our models are not fine-tuned to fit the data; instead, our focus is to reproduce features (1) and (2) from the paragraph above. In fact, the exact dust population cannot be constrained from observations of two wavelengths alone, as scattering polarization depends not only on dust grain sizes, but also on optical depth, albedo, porosity, shape, and temperature. We model the scattering polarization for dust grain populations with maximum radii of 140, 200, and 490  $\mu\text{m}$ , as well as for a disk with two vertically stratified dust grain populations with maximum radii of 140 and 490  $\mu\text{m}$ . The single-population models represent dust populations whose scattering

polarization fractions would peak at 870  $\mu\text{m}$ , 1.3 mm, and 3 mm, respectively, if  $a_{\text{max}} \sim \lambda/2\pi$ , as in Kataoka et al. (2015). For the two-population model, we have chosen dust grain sizes we know will contribute to the scattering polarization at both observed wavelengths. The two-population model is designed as a proof of concept to show that size-dependent dust settling could produce scattering polarization at two widely separated wavelengths, with a higher polarization fraction at the longer wavelength.

For the single-population models, we consider models with a characteristic optical depth ( $\tau_0$ ) of 1 or 10. For each single-grain population model, we also consider two ways of determining the dust scale height: fixing the dust scale height at 10% of the gas scale height, or setting the  $\alpha$  viscosity parameter to a fixed level of  $10^{-3}$  and solving for the dust scale height (Equation (7)). The  $\alpha$  parameter is usually estimated to be  $\sim 10^{-3}$ – $10^{-2}$  from magnetorotational instability (e.g., Simon et al. 2015), but it can also be as low as  $\sim 10^{-4}$ , if the gas is weakly coupled to the magnetic field and hydrodynamical effects like the vertical shear instability dominate (e.g., Flock et al. 2020). Values inferred from observations also produce a wide range, from  $\sim 10^{-5}$  (Villenave et al. 2022) to  $\sim 10^{-4}$ – $10^{-3}$  (e.g., Boneberg et al. 2016; Pinte et al. 2016; Ohashi & Kataoka 2019; Flaherty et al. 2020), and can even be as high as  $\sim 0.08$  (Flaherty et al. 2020). We pick  $10^{-3}$  as a representative value. A viscosity parameter of  $10^{-3}$  yields very similar results to setting  $H_{\text{dust}} = 0.1H_{\text{gas}}$ . Decreasing  $\alpha$  to  $10^{-5}$  decreases the  $H_{\text{dust}}/H_{\text{gas}}$  by a factor of 10, but Ueda et al. (2021) find that size-dependent vertical dust settling occurs for  $\alpha > 10^{-5}$ .

In the two-population model, each dust population is treated as having its own characteristic optical depth; the optical depth of a population is what the optical depth of the disk would be if only that dust grain population were present. The  $\alpha$  viscosity parameter in the two-population model is set to  $10^{-3}$ , and we then solve for the scale height of each dust population. We consider a two-population model in which the characteristic optical depths of the 140  $\mu\text{m}$  and 490  $\mu\text{m}$  populations are 9 and 1, respectively.

We use the radiative transfer code RADMC-3D (Dullemond et al. 2012) to calculate the polarization. Our model assumes compact spherical grains, and we adopt the dust mixture from the Disk Substructures at High Angular Resolution Project (DSHARP), as prescribed in Birnstiel et al. (2018).<sup>7</sup> The composition of the dust (and its refractive index) is water ice (Warren & Brandt 2008), astronomical silicates (Draine 2003), troilite (Henning & Stognienko 1996), and refractory organic material (Henning & Stognienko 1996), with mass fractions of  $\sim 0.2$ , 0.33, 0.07, and 0.4, respectively. For a dust population, the grain size  $a$  follows a power-law distribution, which goes as  $a^{-3.5}$  (Mathis et al. 1977), with cutoffs at a minimum grain size of 0.1  $\mu\text{m}$  and a maximum grain size  $a_{\text{max}}$ , which we treat as a free parameter. Averaging each dust population over a size distribution as opposed to using a single grain size helps produce a smooth scattering matrix and avoids quick oscillations as a function of the scattering angle.

For the disk structure, we parameterize the radial temperature profile as

$$T(r) = 25 \left( \frac{r}{100 \text{ au}} \right)^{-0.5} \text{ K}, \quad (4)$$

<sup>7</sup> The code for calculating the opacity is available at [https://github.com/birnstiel/dsharp\\_opac](https://github.com/birnstiel/dsharp_opac).

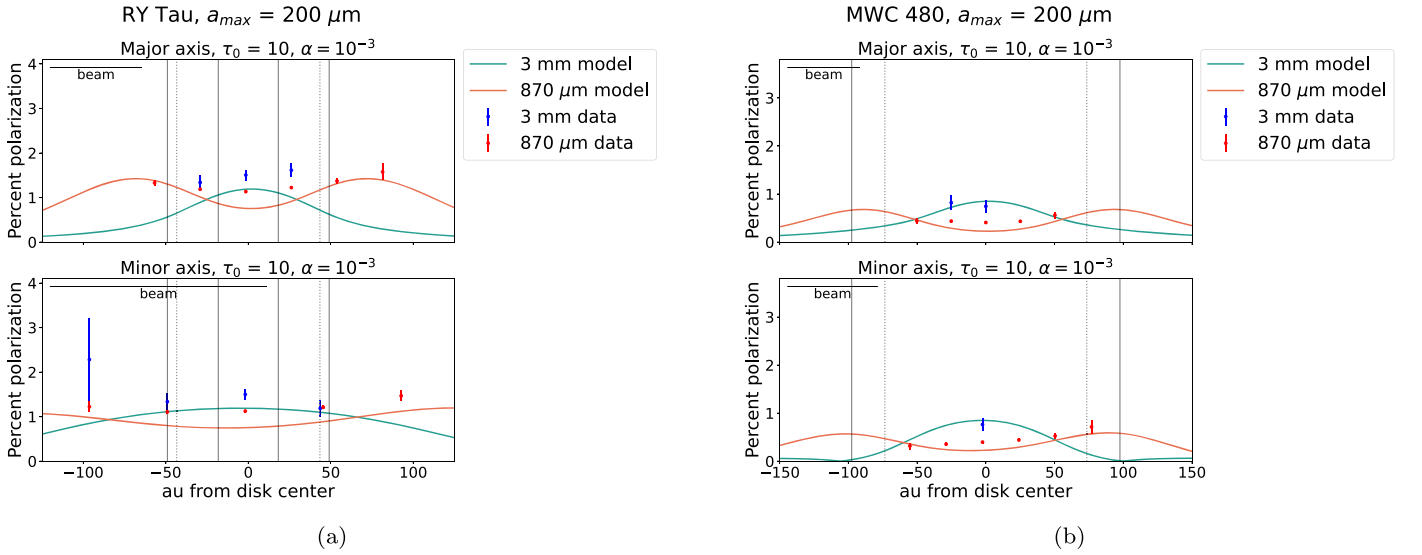


**Figure 6.** Data vs. scattering model with a maximum grain size of  $200 \mu\text{m}$  along the major and minor axes of RY Tau and MWC 480. Models have been convolved with a  $0''.3$  beam.

which is motivated by results from irradiated flared disks in radiative equilibrium (e.g., Chiang & Goldreich 1997). The surface density of the  $i$ th dust population is parameterized by a simple prescription (Lynden-Bell & Pringle 1974):

$$\Sigma_i(r) = \frac{\mu\tau_{0,i}}{\kappa_{\text{ext},i}} \left(\frac{r}{50 \text{ au}}\right)^{-0.5} \exp\left[-\left(\frac{r}{50 \text{ au}}\right)^{1.5}\right], \quad (5)$$

where  $\mu \equiv \cos\theta \cdot \kappa_{\text{ext},i}$  is the extinction opacity and is calculated from the dust model, which, for our case, only depends on  $a_{\text{max}}$ .  $\tau_{0,i}$  is the characteristic optical depth at Band 7 for a given dust population. It is the optical depth at Band 7 (at 50 au, modulated by a factor of  $\sim 0.37$  from the exponential taper, as shown in Equation (5)) if only that one dust population were present and viewed face-on. We treat  $\tau_{0,i}$  as a free parameter for our exploration below.

For simplicity, the vertical density distribution of the  $i$ th grain population follows a Gaussian:

$$\rho_i(r, z) = \frac{\Sigma_i}{\sqrt{2\pi} H_i} \exp\left[-\frac{1}{2}\left(\frac{z}{H_i}\right)^2\right], \quad (6)$$

where  $H_i$  is the dust scale height. We consider dust settling by assuming that dust is in equilibrium between turbulent diffusion and gravitational settling. As such, the dust scale height depends on the size through

$$\frac{H_i}{H_g} = \left(1 + \frac{\text{St} \, 1 + 2\text{St}}{\alpha \, 1 + \text{St}}\right)^{-1/2} \quad (7)$$

(e.g., Dubrulle et al. 1995; Youdin & Lithwick 2007; Ohashi & Kataoka 2019), where St is the Stokes number and  $\alpha$  is the dimensionless parameter that describes the level of turbulence (Shakura & Sunyaev 1973). The gas scale height is simply  $H_g = c_s/\Omega$ , where  $c_s$  is the isothermal sound speed and  $\Omega \equiv \sqrt{GM/r^3}$  is the Keplerian frequency. We adopt  $M = 2M_\odot$ , which is representative of MWC 480 and RY Tau (Long et al. 2018). The Stokes number of the grains in a disk depends on the surface density of the gas through (e.g.,

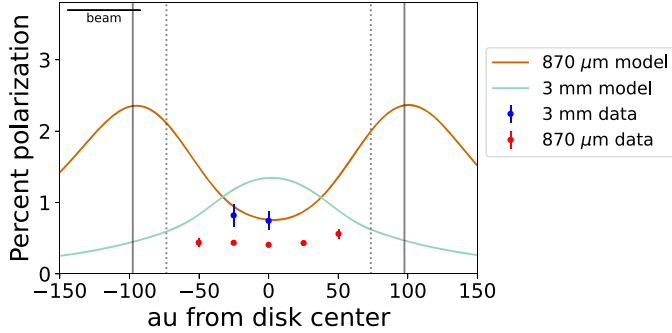
Dullemond et al. 2018)

$$\text{St} = \frac{\pi \rho_s a}{2 \Sigma_g}, \quad (8)$$

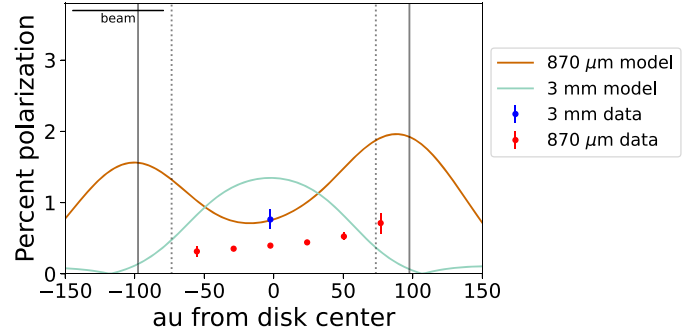
where  $\rho_s$  is the specific weight of the dust mixture (which is  $\sim 1.68 \text{ g cm}^{-3}$  for the DSHARP composition) and  $a$  is the grain size that we use for  $a_{\text{max}}$  for the corresponding dust population. The gas surface density  $\Sigma_g$  is the summation of each dust surface density  $\Sigma_i$  times the gas-to-dust mass ratio of 100.

The model images used for RY Tau have an inclination of  $\theta = 65^\circ$  and those for MWC 480 have  $\theta = 37^\circ$ . To account for finite resolution, each model image is convolved with a  $0''.3$  circular beam.

Figures 6 and 7 show the models that produce a detectable degree of polarization at both wavelengths and a higher polarization fraction at 3 mm at the center of the disk. In these figures, as well as the figures in the Appendix, distances along the minor axis have been deprojected to account for the disks' inclination angles. The radial locations of features seen in the models are different along the major and minor axes, because the larger deprojected beam FWHM along the minor axis smears out features. In both MWC 480 and RY Tau, the single-population scattering model with a maximum dust grain size of  $200 \mu\text{m}$  reproduces the key features. The two-population model also reproduces the key features in MWC 480. We note that the effects of dust grain size and optical depth on scattering polarization are degenerate to some extent; high optical depth can decrease the observed polarization fraction from the theoretical maximum value, but so can a maximum dust grain size smaller or larger than the size that would produce the highest polarization fraction at a given observing wavelength. For example, in MWC 480, the two-population model overpredicts the polarization fraction at both wavelengths. Because the effects of optical depth and dust grain size on scattering polarization are somewhat degenerate when data are only available at two wavelengths, adjusting either the optical depths or the maximum dust grain sizes could bring the model results closer to the observed polarization fractions. Future polarization observations at wavelengths between  $870 \mu\text{m}$  and

MWC 480 major axis, 140+490  $\mu\text{m}$  grains

(a)

MWC 480 minor axis, 140+490  $\mu\text{m}$  grains

(b)

**Figure 7.** Data vs. scattering model with maximum grain sizes of 140 and 490  $\mu\text{m}$  along the major and minor axes of MWC 480. Models have been convolved with a  $0''.3$  beam.

3 mm, as well as higher-resolution, higher-sensitivity observations, would allow us to fine-tune our models.

Although our models fit the general trends, they could be brought into closer detailed agreement with the observations by changing the maximum dust grain size(s) to values between 140 and 200  $\mu\text{m}$  or between 200 and 490  $\mu\text{m}$ . Increasing the total optical depth to the point where the polarization fraction is attenuated as the radiation field incident on a grain becomes more isotropic could also bring the model polarization fractions in Figures 6 and 7 closer to the observations. Additionally, larger ( $\sim$ millimeter-sized) compact dust aggregates could produce an observable degree of scattering polarization at both 3 mm and 870  $\mu\text{m}$ , as presented in Tazaki et al. (2019). Future efforts including comparing models of the Stokes  $I$  for these dust populations to the observed Stokes  $I$  of these disks individually would be valuable for constraining the dust properties of each source.

In the Appendix, we compare the data to the full suite of models. As seen in Figures 8 and 9, models in which the maximum dust grain size is 140  $\mu\text{m}$  or 490  $\mu\text{m}$  produce a significant degree of polarization at 870  $\mu\text{m}$  and 3 mm, respectively, but not at the other wavelength. In models in which the dust grains have a maximum radius of 200  $\mu\text{m}$ , both wavelengths show polarization fractions that would be detectable with ALMA. However, only the model with a higher characteristic optical depth ( $\tau_0 = 10$ ) shows a higher polarization fraction at 3 mm than at 870  $\mu\text{m}$  at the center of the disk (see Figures 10 and 11). The dip in polarization fraction in the center of the disk at shorter wavelengths is due to optical depth effects. As the disk becomes more optically thick, the incident radiation field becomes more isotropic, and the net polarization fraction from scattering decreases (Yang et al. 2017). In the two-population model, a degree of polarization that would be observable with ALMA is produced at both wavelengths in both disks. In MWC 480, the two-population model produces a higher polarization fraction at 3 mm in the center of the disk, while the polarization fraction remains higher at 870  $\mu\text{m}$  in the center of the disk in RY Tau (see Figure 12).

One possible origin for two size populations at a given radius is that one population could be originally associated with the local gas while the other could be dust that has drifted radially (relative to the gas) to that radius. Numerical simulations with detailed dust physics (including growth, fragmentation, radial drift, and vertical settling) are needed to determine whether a

disk could host a bimodal dust population. The assumed size distribution of the dust grains would affect the expected polarization fractions. For example, Ueda et al. (2021) modeled the scattering polarization in HL Tau for Mathis, Rumpl, and Nordsieck (MRN; Mathis et al. 1977) distributions of dust grain sizes with different maximum sizes and different levels of turbulence. They found that if the dust grain sizes have an MRN distribution with a single maximum size, then grains with a maximum radius of size of  $\lesssim 1$  mm and turbulence strength parameter of  $\lesssim 10^{-5}$  could explain the polarization seen at 870  $\mu\text{m}$  and 1.3 mm, as well as the disk's spectral energy distribution.

#### 4.2. Polarization Spectra

The disks in this survey exhibit clear differences in the correlation between polarization morphology and observing wavelength. This may indicate differences in the disks' dust grain sizes or dust optical depths, or it could arise from differences in protostar luminosities. In this section, we examine each of these cases.

Lin et al. (2022) found that the transition between the azimuthal polarization morphology seen in sources such as HL Tau, DG Tau, and Haro 6-13 at 3 mm (which likely arises from dichroic emission of aligned grains) and the scattering polarization seen at 870  $\mu\text{m}$  in the same source could be explained by optical depth effects. Optical depth influences which polarization mechanism dominates the polarized emission produced at a given wavelength. At low optical depths, the probability that a photon will encounter a dust grain and scatter to produce polarization is low. Therefore, the scattering polarization tends to be weaker than any polarization from direct thermal emission from aligned dust grains. At high optical depths, photons are likely to encounter aligned dust grains, which preferentially absorb light whose E-vector is along their long axes. This preferential absorption, known as dichroic extinction, reduces the amount of polarized emission from thermal emission from aligned grains. On the other hand, high optical depths mean that a photon is likely to encounter a dust grain and scatter, thus raising the amount of scattering polarization. The scattering polarization at high optical depths is the net result of multiple scattering events.

While the transition between azimuthal and scattering polarization occurs between 3 mm and 870  $\mu\text{m}$  in Haro 6-13 and V892 Tau, RY Tau and MWC 480 are still both consistent

with scattering at 3 mm. Given the relationship between polarization morphology and optical depth described in Lin et al. (2022), we expect that if there are aligned grains in RY Tau and MWC 480, the transition between thermal and scattering polarization will occur at wavelengths longer than 3 mm. Compared to Haro 6-13, RY Tau and MWC 480 also have brighter disks, which are likely to have higher optical depths and thus a stronger scattering at 3 mm. V892 Tau’s disk is brighter still, but its dust polarization may be affected by a large hole surrounding the binary system. It is also interesting to note that RY Tau and MWC 480 have stellar masses significantly higher than that of Haro 6-13 ( $\sim 2M_{\odot}$  versus  $\sim 1M_{\odot}$ ).

Other possible reasons for the differences in polarization morphology between the disks are that Haro 6-13 and V892 Tau do not contain dust grains large enough to efficiently create scattering polarization at 3 mm and that the population of large dust grains in these sources is optically thin. We speculate that RY Tau and MWC 480 may have higher optical depths than Haro 6-13 due to their polarization spectra. If the transition between scattering and the azimuthal polarization pattern is controlled by optical depth, as explored in Lin et al. (2022), then disks with higher optical depths would transition from showing polarization consistent with scattering to showing azimuthal polarization at longer wavelengths. Observing these disks in polarization at wavelengths longer than 3 mm would allow us to determine where the change in polarization morphology occurs in RY Tau and MWC 480.

As described in Tram & Hoang (2022), the RAT acting on a grain is directly proportionate to the energy density of the radiation field. A more luminous protostar would therefore create a stronger RAT, leading to a higher probability of radiatively aligned grains. V892 Tau is the most luminous source in our sample (see Table 1) and shows a transition between an azimuthal polarization morphology at 3 mm and a morphology consistent with scattering at  $870 \mu\text{m}$ . RY Tau and MWC 480 are more luminous than Haro 6-13, but are consistent with scattering at both wavelengths, while Haro 6-13 shows the same transition of polarization morphologies as V892 Tau. All else being equal, we would expect higher protostar luminosities to lead to more polarization from radiative alignment, but other differences between the systems may have more influence on their polarization morphologies. DL Tau’s disk is less bright than those of RY Tau and MWC 480, and its protostar’s luminosity is  $0.65 L_{\odot}$ . DL Tau’s polarization morphology cannot be conclusively determined from the tentative detection of polarization at 3 mm, since the polarized region was smaller than a beam, allowing for only one measurement of the polarization fraction and angle. If the polarized emission at 3 mm is real, then DL Tau’s polarization spectrum resembles those of RY Tau and MWC 480. However, higher-sensitivity observations are needed to determine whether DL Tau has more extended polarized emission at 3 mm. Determining whether stellar mass and luminosity are correlated with polarization spectrum will require multi-wavelength polarization observations of a wider sample of disks.

## 5. Conclusions

In this multiwavelength survey of dust polarization in protoplanetary disks, we have shown that Class II disks in the same molecular cloud can exhibit different transitions

between polarization morphologies at observing wavelengths of 3 mm and  $870 \mu\text{m}$ . The transition between azimuthal and scattering polarization in Haro 6-13 and V892 Tau can be explained by how optical depth affects whether a source’s observed polarization comes primarily from the thermal emission of aligned grains or self-scattering. Polarization observations at wavelengths longer than 3 mm, possibly with the Next Generation Very Large Array, will be needed to locate where the transition between the two polarization morphologies occurs in RY Tau and MWC 480.

In contrast to Haro 6-13 and V892 Tau, the polarized emission in RY Tau and MWC 480 is consistent with scattering at both wavelengths. Using models of scattering polarization, we aimed to determine what dust grain population(s) could produce a significant polarization fraction at both wavelengths and a polarization fraction that was higher at 3 mm than at  $870 \mu\text{m}$  in the center of the disk. We found that in RY Tau, dust grains with a maximum radius ( $a_{\text{max}}$ ) of  $200 \mu\text{m}$  and an optical depth at 50 au ( $\tau_0$ ) of 10 could reproduce these features. In MWC 480, the model with  $a_{\text{max}} = 200 \mu\text{m}$  and  $\tau_0 = 10$  could reproduce the key features. The model with large grains ( $a_{\text{max}} = 490 \mu\text{m}$ ,  $\tau_0 = 1$ ) near the midplane and small grains ( $a_{\text{max}} = 140 \mu\text{m}$  and  $\tau_0 = 9$ ) above and below the midplane can also reproduce the key features in MWC 480. With two observing wavelengths, the effects of dust grain size and optical depth (i.e., dust grain number density) on the observed polarization are still somewhat degenerate. The region of degeneracy shrinks as the source is observed at more wavelengths, providing stricter constraints on dust grain properties.

## Acknowledgments

This paper makes use of the following ALMA data: ALMA #2017.1.00470.S. ALMA is a partnership of ESO (representing its member states), NSF (USA) and NINS (Japan), together with NRC (Canada), MOST and ASIAA (Taiwan), and KASI (Republic of Korea), in cooperation with the Republic of Chile. The Joint ALMA Observatory is operated by ESO, AUI/NRAO, and NAOJ. The National Radio Astronomy Observatory is a facility of the National Science Foundation operated under cooperative agreement by Associated Universities, Inc. We thank the anonymous reviewer, whose comments helped to strengthen this manuscript. R.E.H. and L.W.L. acknowledge support from NSF AST-1910364. L.W.L. acknowledges support from NSF AST-1910364 and NSF AST-2307844. R.E.H. also acknowledges support from the ALMA Student Observing Support (SOS). Z.Y.D.L. acknowledges support from the Jefferson Foundation, NASA 80NSSC18K1095, and also support from the ALMA Student Observing Support (SOS). Z.Y.L. is supported in part by NASA 80NSSC20K0533 and NSF AST-1910106.

## Appendix

Here, we compare the  $870 \mu\text{m}$  and 3 mm polarization data for MWC 480 and RY Tau to the full range of scattering models we created. As stated in Section 4.1, the goal of this modeling is not to find a dust population that fits all features seen in the data, but to provide a proof of concept that it is important to consider optical depth effects and dust settling when using scattering polarization observations to constrain dust grain sizes. The polarization fractions are generally higher

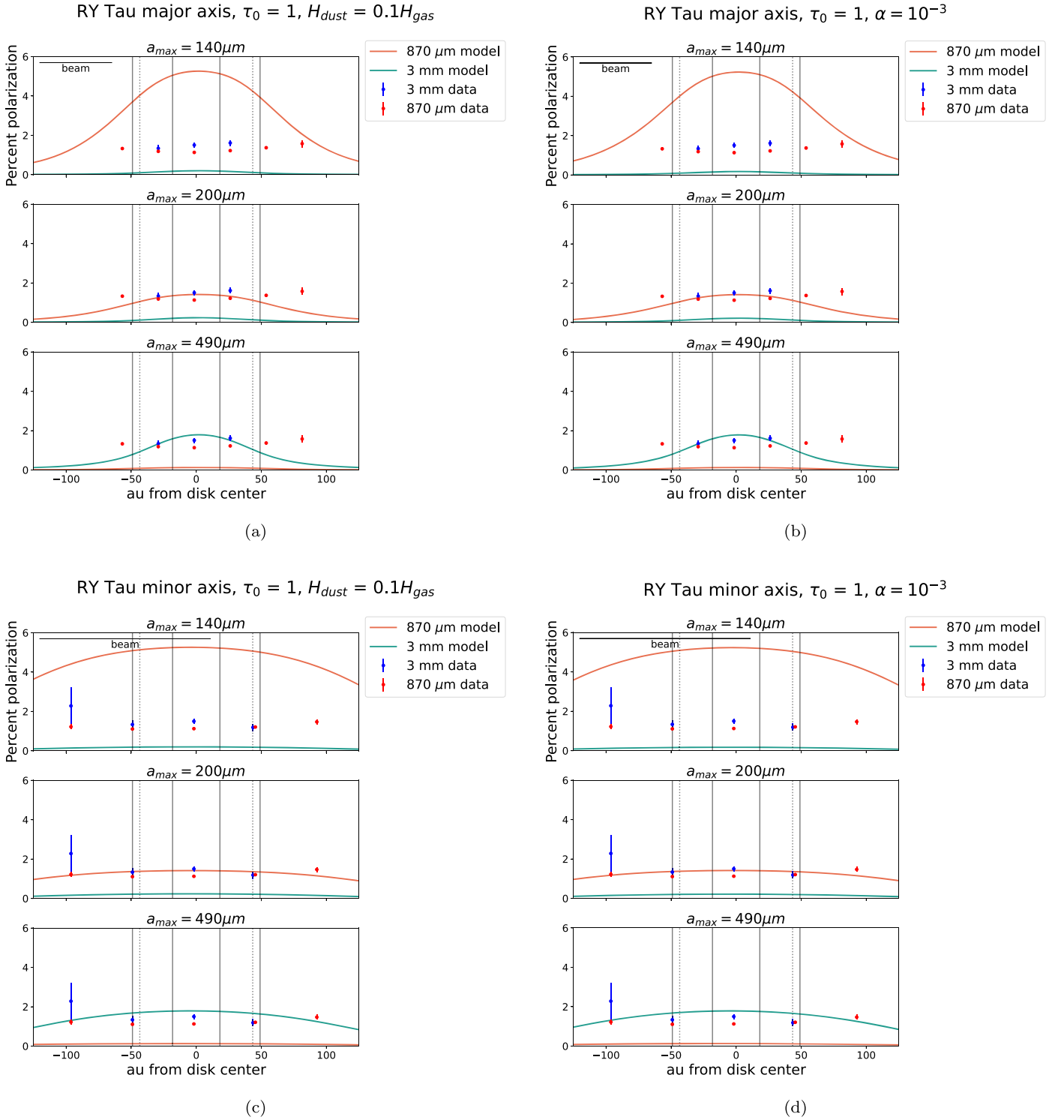


**Figure 8.** Data vs.  $\tau_0 = 1$  single-grain scattering models along the major and minor axes of RY Tau. Models have been convolved with a  $0''.3$  beam. The solid gray lines represent the locations of rings, and the dashed gray lines represent the locations of gaps from Long et al. (2018). The beam scale bar represents the beam major axis of the 3 mm data.

for RY Tau than for MWC 480 due to inclination-induced polarization (Yang et al. 2016). We find that, generally, models including a single dust grain population with a maximum grain size of  $140 \mu\text{m}$  or  $490 \mu\text{m}$  are not good fits to the data.

At low optical depths ( $\tau_0 = 1$ ), the  $140 \mu\text{m}$  dust efficiently produces polarized emission at  $870 \mu\text{m}$ , but produces very low polarization fractions at 3 mm and vice versa for the  $490 \mu\text{m}$

dust (see the top and bottom panels, respectively, of Figures 8 and 9). The polarization fractions produced at  $870 \mu\text{m}$  and 3 mm by the  $a_{\text{max}} = 200 \mu\text{m}$  model with low optical depth are more similar to one another; however, this model still produces a higher polarization fraction at  $870 \mu\text{m}$  than at 3 mm in the center of the disk, contrary to the data (see the middle panels of Figures 8 and 9). None of the models with low characteristic

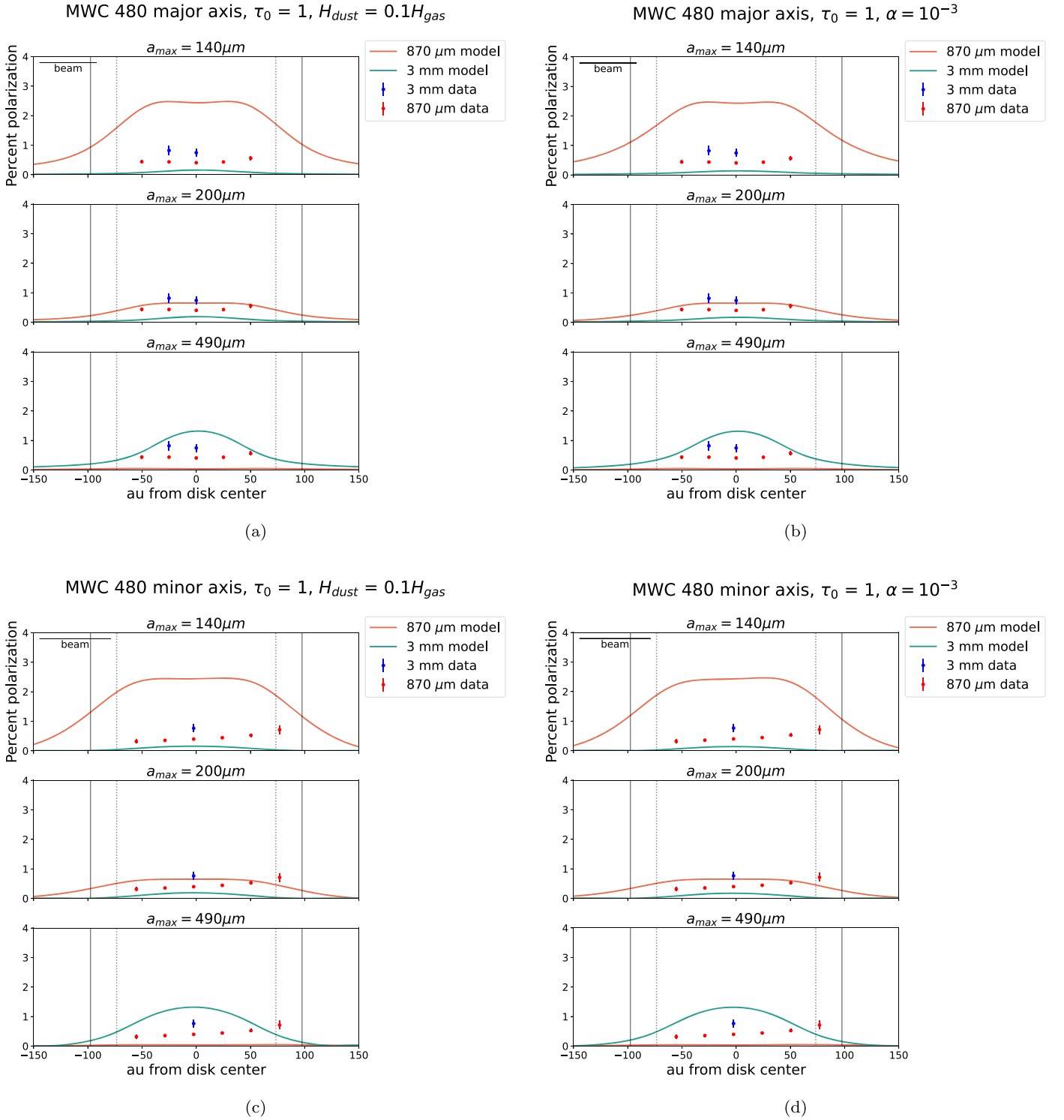


**Figure 9.** Data vs.  $\tau_0 = 1$  single-grain scattering models along the major and minor axes of MWC 480. Models have been convolved with a  $0''.3$  beam. The solid gray lines represent the locations of rings, and the dashed gray lines represent the locations of gaps from Long et al. (2018). The beam scale bar represents the beam major axis of the 3 mm data.

optical depth and a single dust grain population reproduce the relative polarization fractions seen in the data. Therefore, we have explored models with high characteristic optical depths and multiple dust grain populations.

At high characteristic optical depths ( $\tau_0 = 10$ ), the  $140 \mu\text{m}$  dust can produce polarization fractions of up to  $\sim 1\%$  in RY Tau and up to  $\sim 0.5\%$  in MWC 480 (see Figures 10 and 11). At

high optical depths, the incident radiation field on a dust grain becomes increasingly isotropic, which attenuates the observed polarization fraction (Yang et al. 2017). This effect can be observed in the dip in polarization fraction at  $870 \mu\text{m}$  at the center of the disk for models with high characteristic optical depths (see the top and middle panels of Figures 10 and 11). The dip in polarization fraction at the center of the disk is

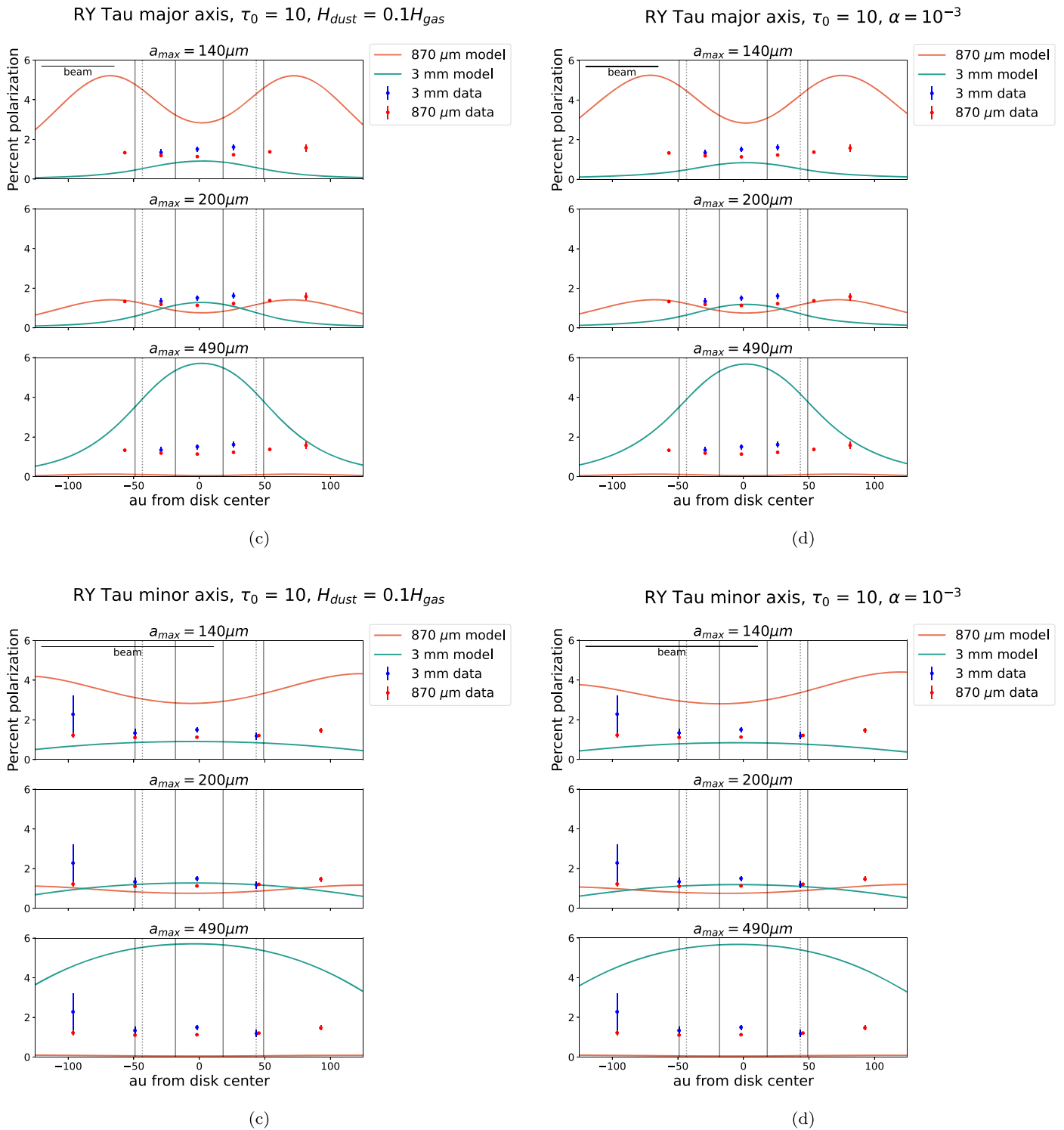


**Figure 10.** Data vs.  $\tau_0 = 10$  single-grain scattering models along the major and minor axes of RY Tau. Models have been convolved with a  $0''.3$  beam. The solid gray lines represent the locations of rings, and the dashed gray lines represent the locations of gaps from Long et al. (2018). The beam scale bar represents the beam major axis of the 3 mm data.

present in the  $870\ \mu\text{m}$  data, which indicates that high-optical-depth models should be explored. The high-optical-depth models with  $a_{\text{max}} = 490\ \mu\text{m}$  produce a higher polarization fraction at 3 mm than at  $870\ \mu\text{m}$  at the center of the disk, but they produce a very low polarization fraction at the shorter wavelength (see the bottom panels of Figures 10 and 11). The high-optical-depth models with  $a_{\text{max}} = 200\ \mu\text{m}$  produce a

significant polarization fraction at both wavelengths and have a higher polarization fraction at 3 mm than at  $870\ \mu\text{m}$  at the center of the disk (see the middle panels of Figures 10 and 11). These comparisons of the single-population, high-optical-depth models to the data indicate that future work should explore dust populations with maximum sizes between those with size parameters of 1 at 3 mm and  $870\ \mu\text{m}$ .

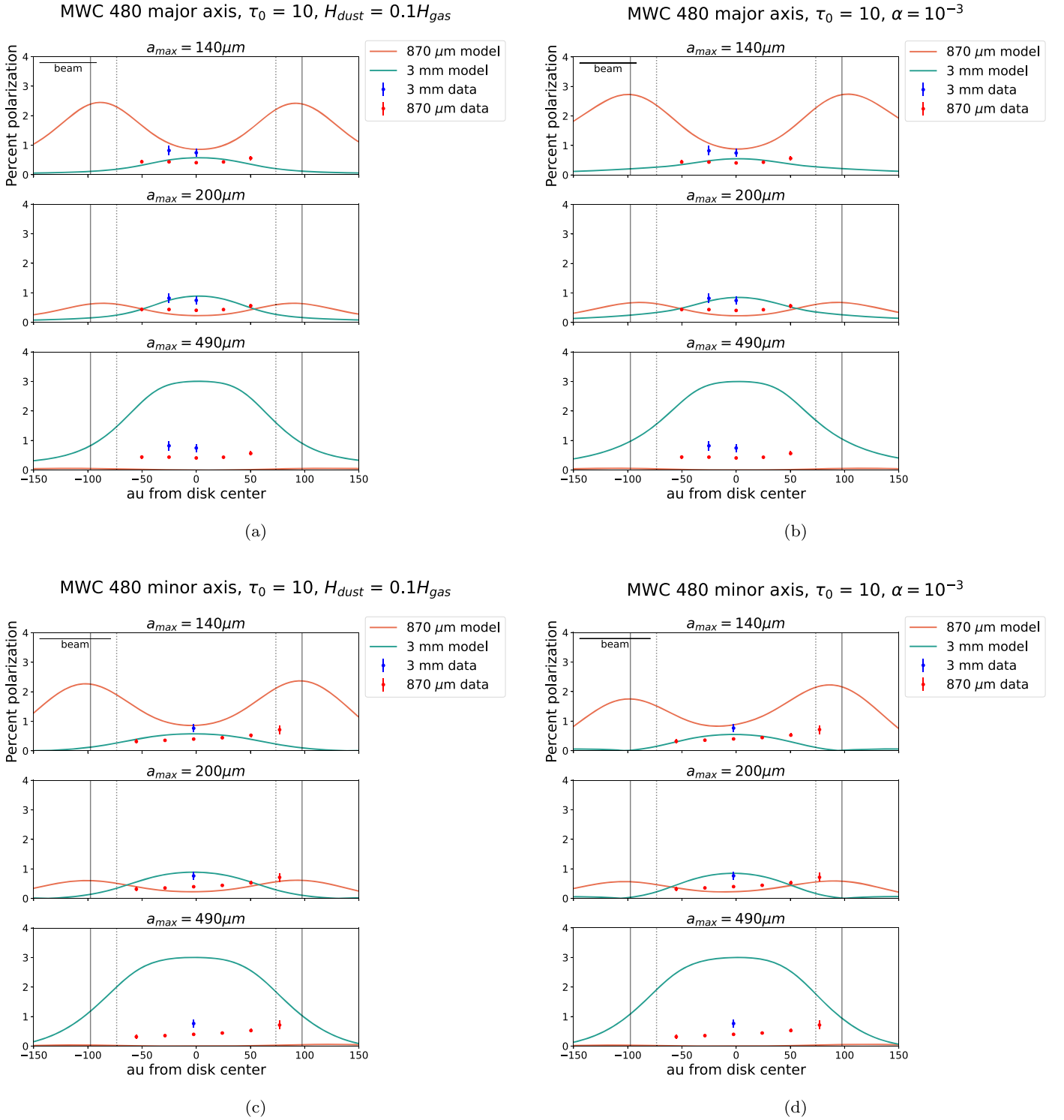


**Figure 11.** Data vs.  $\tau_0 = 10$  single-grain scattering models along the major and minor axes of MWC 480. Models have been convolved with a  $0''.3$  beam. The solid gray lines represent the locations of rings, and the dashed gray lines represent the locations of gaps from Long et al. (2018). The beam scale bar represents the beam major axis of the 3 mm data.

Theoretical work (e.g., Ueda et al. 2021) and observations (e.g., Lee et al. 2017) both indicate that size-dependent vertical dust settling occurs in protoplanetary disks. This vertical stratification of dust by size would affect the scattering polarization, as described in Section 4. As a proof of concept, we present models of the scattering polarization resulting from 490  $\mu\text{m}$  dust near the disk midplane and 140  $\mu\text{m}$  dust above

and below the midplane. In a disk with the inclination of RY Tau, this dust population produces a polarization fraction that would be observable at both 870  $\mu\text{m}$  and 3 mm. However, the polarization fraction would be higher at 870  $\mu\text{m}$  at the center of the disk, which is the opposite of the pattern seen in the data (see Figures 12(a) and (b)). For a disk with the inclination of MWC 480, this dust population leads to higher polarization



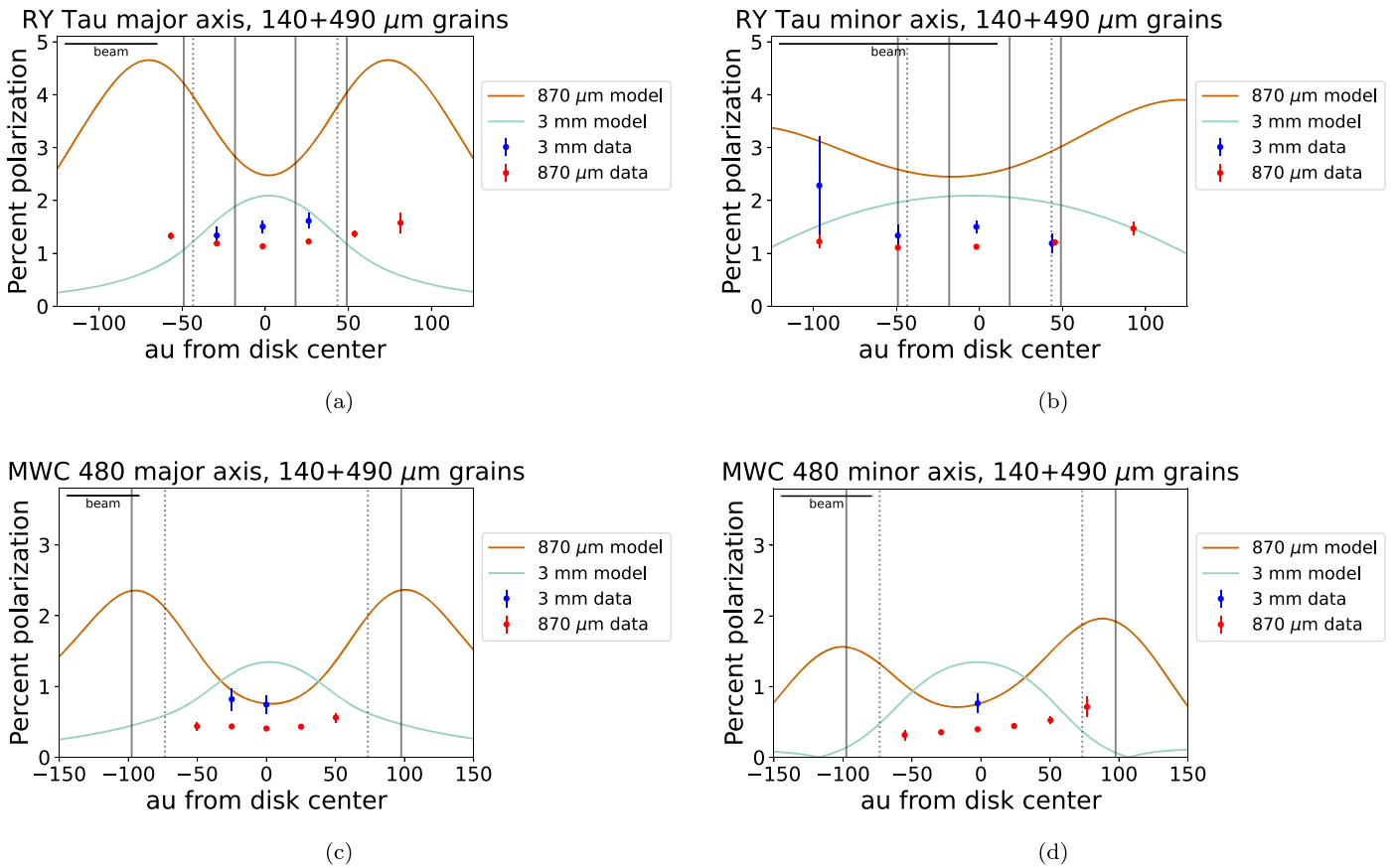


**Figure 12.** Data vs. models including two dust populations with maximum grain radii of 140 and 490  $\mu\text{m}$  along the major and minor axes of MWC 480 and RY Tau. Models have been convolved with a  $0''.3$  beam. The solid gray lines represent the locations of rings, and the dashed gray lines represent the locations of gaps from Long et al. (2018). The beam scale bar represents the beam major axis of the 3 mm data.

fraction at 3 mm at the center of the disk (see Figures 12(c) and (d)).

### ORCID iDs

Rachel E. Harrison <https://orcid.org/0000-0003-2118-4999>  
 Zhe-Yu Daniel Lin <https://orcid.org/0000-0001-7233-4171>  
 Leslie W. Looney <https://orcid.org/0000-0002-4540-6587>  
 Zhi-Yun Li <https://orcid.org/0000-0002-7402-6487>  
 Haifeng Yang <https://orcid.org/0000-0002-8537-6669>  
 Ian W. Stephens <https://orcid.org/0000-0003-3017-4418>  
 Manuel Fernández-López <https://orcid.org/0000-0001-5811-0454>

### References

- Alves, F. O., Girart, J. M., Padovani, M., et al. 2018, *A&A*, 616, A56  
 Bacciotti, F., Girart, J. M., Padovani, M., et al. 2018, *ApJL*, 865, L12  
 Barrière-Fouchet, L., Gonzalez, J. F., Murray, J. R., Humble, R. J., & Maddison, S. T. 2005, *A&A*, 443, 185  
 Birstiel, T., Dullemond, C. P., Zhu, Z., et al. 2018, *ApJL*, 869, L45  
 Boneberg, D. M., Panić, O., Haworth, T. J., Clarke, C. J., & Min, M. 2016, *MNRAS*, 461, 385  
 Brunngräber, R., & Wolf, S. 2020, *A&A*, 640, A122  
 Chiang, E. I., & Goldreich, P. 1997, *ApJ*, 490, 368  
 Dent, W. R. F., Pinte, C., Cortes, P. C., et al. 2019, *MNRAS*, 482, L29  
 Draine, B. T. 2003, *ARA&A*, 41, 241  
 Dubrulle, B., Morfill, G., & Sterzik, M. 1995, *Icar*, 114, 237  
 Dullemond, C. P., Birstiel, T., Huang, J., et al. 2018, *ApJL*, 869, L46  
 Dullemond, C. P., Juhasz, A., Pohl, A., et al. 2012, RADMC-3D: A Multi-purpose Radiative Transfer Tool, Astrophysics Source Code Library, ascl:1202.015  
 Flaherty, K., Hughes, A. M., Simon, J. B., et al. 2020, *ApJ*, 895, 109  
 Flock, M., Turner, N. J., Nelson, R. P., et al. 2020, *ApJ*, 897, 155  
 Gaia Collaboration, Brown, A. G. A., Vallenari, A., et al. 2016, *A&A*, 595, A2  
 Gaia Collaboration, Mignard, F., Klioner, S. A., et al. 2018, *A&A*, 616, A14  
 Garufi, A., Podio, L., Codella, C., et al. 2021, *A&A*, 645, A145  
 Gold, T. 1952, *MNRAS*, 112, 215  
 Hamidouche, M. 2010, *ApJ*, 722, 204  
 Harrison, R. E., Looney, L. W., Stephens, I. W., et al. 2019, *ApJL*, 877, L2  
 Henning, T., & Stognienko, R. 1996, *A&A*, 311, 291  
 Herczeg, G. J., & Hillenbrand, L. A. 2014, *ApJ*, 786, 97  
 Kataoka, A., Muto, T., Momose, M., et al. 2015, *ApJ*, 809, 78  
 Kataoka, A., Okuzumi, S., & Tazaki, R. 2019, *ApJL*, 874, L6  
 Kataoka, A., Tsukagoshi, T., Pohl, A., et al. 2017, *ApJL*, 844, L5  
 Lazarian, A. 2007, *JQSRT*, 106, 225  
 Lee, C.-F., Li, Z.-Y., Ho, P. T. P., et al. 2017, *SciA*, 3, e1602935  
 Lin, Z.-Y. D., Li, Z.-Y., Stephens, I. W., et al. 2024, *MNRAS*, 528, 843  
 Lin, Z.-Y. D., Li, Z.-Y., Yang, H., et al. 2020, *MNRAS*, 496, 169  
 Lin, Z.-Y. D., Li, Z.-Y., Yang, H., et al. 2022, *MNRAS*, 512, 3922  
 Long, F., Andrews, S. M., Vega, J., et al. 2021, *ApJ*, 915, 131  
 Long, F., Herczeg, G. J., Harsono, D., et al. 2019, *ApJ*, 882, 49  
 Long, F., Pinilla, P., Herczeg, G. J., et al. 2018, *ApJ*, 869, 17  
 Lynden-Bell, D., & Pringle, J. E. 1974, *MNRAS*, 168, 603  
 Mathis, J. S., Rumpl, W., & Nordsieck, K. H. 1977, *ApJ*, 217, 425  
 Ohashi, S., & Kataoka, A. 2019, *ApJ*, 886, 103  
 Ohashi, S., Kataoka, A., Nagai, H., et al. 2018, *ApJ*, 864, 81  
 Pinte, C., Dent, W. R. F., Ménard, F., et al. 2016, *ApJ*, 816, 25  
 Rao, R., Girart, J. M., Lai, S.-P., & Marrone, D. P. 2014, *ApJL*, 780, L6  
 Sadavoy, S. I., Myers, P. C., Stephens, I. W., et al. 2018, *ApJ*, 859, 165  
 Sadavoy, S. I., Stephens, I. W., Myers, P. C., et al. 2019, *ApJS*, 245, 2  
 Schaefer, G. H., Dutrey, A., Guilloteau, S., Simon, M., & White, R. J. 2009, *ApJ*, 701, 698  
 Segura-Cox, D. M., Looney, L. W., Stephens, I. W., et al. 2015, *ApJL*, 798, L2  
 Shakura, N. I., & Sunyaev, R. A. 1973, *A&A*, 24, 337  
 Simon, J. B., Hughes, A. M., Flaherty, K. M., Bai, X.-N., & Armitage, P. J. 2015, *ApJ*, 808, 180  
 Stephens, I. W., Looney, L. W., Kwon, W., et al. 2014, *Natur*, 514, 597

- Stephens, I. W., Yang, H., Li, Z.-Y., et al. 2017, *ApJ*, 851, 55
- Tazaki, R., Lazarian, A., & Nomura, H. 2017, *ApJ*, 839, 56
- Tazaki, R., Tanaka, H., Kataoka, A., Okuzumi, S., & Muto, T. 2019, *ApJ*, 885, 52
- Tram, L. N., & Hoang, T. 2022, *FrASS*, 9, 923927
- Ueda, T., Kataoka, A., Zhang, S., et al. 2021, *ApJ*, 913, 117
- Vidal, M., Leahy, J. P., & Dickinson, C. 2016, *MNRAS*, 461, 698
- Villenave, M., Stapelfeldt, K. R., Duchêne, G., et al. 2022, *ApJ*, 930, 11
- Wardle, J. F. C., & Kronberg, P. P. 1974, *ApJ*, 194, 249
- Warren, S. G., & Brandt, R. E. 2008, *JGRD*, 113, D14220
- Yang, H., Li, Z.-Y., Looney, L., & Stephens, I. 2016, *MNRAS*, 456, 2794
- Yang, H., Li, Z.-Y., Looney, L. W., Girart, J. M., & Stephens, I. W. 2017, *MNRAS*, 472, 373
- Yang, H., Li, Z.-Y., Stephens, I. W., Kataoka, A., & Looney, L. 2019, *MNRAS*, 483, 2371
- Youdin, A. N., & Lithwick, Y. 2007, *Icar*, 192, 588